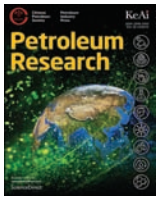
Petroleum Research 11 (2026) 297–308

Contents lists available at ScienceDirect

Petroleum Research

journal homepage: http://www.keaipublishing.com/en/journals/petroleum-research/



Full Length Article

Oil flow impact characteristics of internal floating roof tanks during floating roof landing and oil receiving processes



Yan Li [a, b, *], Chunqiang Zhu [c], Fulin Yang [a, b], Xinpeng Wang [a, b], Jieyao Jia [a, b]

[a] Guangxi Key Laboratory of Green Chemical Materials and Safety Technology, Beibu Gulf University, Qinzhou, 535011, China
[b] Guangxi Key Laboratory of Ocean Engineering Equipment and Technology, Beibu Gulf University, Qinzhou 535011, China
[c] Guangxi Petrochemical Company, PetroChina, Qinzhou, 535000, China

ARTICLE INFO

Article history:
Received 27 November 2024
Received in revised form
19 May 2025
Accepted 25 May 2025
Available online 6 June 2025

Keywords:
Internal floating roof tanks
Turbulence
Impact
Floating roof
Influence characteristics

ABSTRACT

To maintain the integrity of internal floating roof tanks, curb environmental pollution and guarantee the safety of tank farms, it is important to determine the oil flow features that impact the floating roof during the oil receiving process, especially when the floating roof falls to the bottom of the tank. In this study, the finite volume, volume of fluid (VOF), and realizable k-ε turbulence models and the pressure implicit with splitting of operators (PISO) algorithm were adopted to establish a three-dimensional physical model of an internal floating roof tank and simulate the oil receiving process. A pressure test platform was then set up to validate the model's viability. The flow field characteristics and influencing properties of the impact of the liquid against the floating roof under different oil inlet velocities, initial liquid levels, medium densities, and tank diameters were analyzed and compared. The results showed that increasing the oil inlet velocity and medium density led to the maximum pressure and the impact force at different moments of the liquid against the floating roof also increasing. An increase in the oil inlet velocity, led to greater turbulence on the opposite the inlet, and higher pressure at the edge of the floating roof in the upper area opposite the inlet. At an oil inlet velocity of 4.0 m/s, the maximum pressure was 135.5 kPa and the maximum impact force peak was 13.967 MN. The initial liquid level increase had little influence on the liquid's impact on the floating roof, and the high pressure zone was at the edge of the floating roof opposite the inlet. When the initial level was 0.5 m, the maximum pressure was 135.81 kPa and the maximum impact force peak was 14.021 MN. As the density of the medium increased, the greater the turbulence on the inlet relative side and the higher pressure at the edge of the floating roof in the upper area of the inlet relative side. When diesel was the medium, the maximum pressure was 154.9 kPa and the maximum impact force peak was 15.999 MN. As the diameter of the tank increased, the maximum pressure of the floating roof impacted by the liquid reduced, but the impact force increased. The slower the turbulence on the inlet relative side, the greater the maximum pressure zone of the floating roof. When the tank volume was 1000 m^3, the maximum pressure was 135.5 kPa. When the tank volume was 10,000 m^3, the maximum impact force peak was 81.978 MN. Considering the above, a low velocity, a low-density light oil, and an internal floating roof tank with a small diameter are recommended for engineering operations that involve receiving oil. Further increased safety precautions at the edge of the floating roof opposite the inlet are needed. In sum, the findings of the study offer theoretical justifications and a technical reference for optimizing the structural design of floating roofs and the oil receiving and delivering process.

© 2025 Chinese Petroleum Society. Publishing services by Elsevier B.V. on behalf of KeAi Communications Co. Ltd. This is an open access article under the CC BY license (http://creativecommons.org/licenses/by/4.0/).

1. Introduction

Internal floating roof tanks are frequently utilized in oil refinery depots, oil product transfer depots, and oil product sales depots for the storage of high volatile oils, such as gasoline, kerosene, diesel, and naphtha (Kwon et al., 2021; Yang et al., 2024). However, if the liquid level inside a tank is low during oil receiving operations, turbulence is caused, impacting the floating roof with an uneven force and causing a large area of damage. This leads to the oil and gas diffusing to the space created by the damaged area of the floating roof below the top of the tank and then leaking to the atmosphere through the vent, thus resulting in a waste of resources

* Corresponding author. Guangxi Key Laboratory of Green Chemical Materials and Safety Technology, Beibu Gulf University, Qinzhou, 535011, China.
E-mail address: liyan@bbgu.edu.cn (Y. Li).
Peer review under the responsibility of Editorial Office of Petroleum Research.

https://doi.org/10.1016/j.ptlrs.2025.05.006
2096-2495/© 2025 Chinese Petroleum Society. Publishing services by Elsevier B.V. on behalf of KeAi Communications Co. Ltd. This is an open access article under the CC BY license (http://creativecommons.org/licenses/by/4.0/).

and a great amount of environmental pollution (Li et al., 2024). On June 13, 2017, the aluminum floating roof of a 10,000 m^3 gasoline tank owned by PetroChina Guangxi Petrochemical Company was damaged and fell to the bottom (Zhao, 2020), resulting in a large amount of oil and gas leakage (see Fig. 1). Further, lightning strikes or electrostatic induction from thunderclouds can cause fire and explosions (Adekitan and Rock, 2022; Neyshabouri and Niasati, 2024), resulting in serious economic losses (Zhou et al., 2023). To guarantee the integrity of such tanks and ensure the safety and reliability of storage and transportation systems, it is crucial to determine the direct causes and impact mechanisms of tank explosion accidents (Burmana et al., 2024). Oil receiving operations have adopted measures such as lowering the oil inlet velocity and using a highly stable floating roof, but accidents due to broken floating roofs and floating roofs falling to the bottom still occur from time to time. Floating roofs may also remain at the 1.8 m position instead of going with the oil lifting movement, and the associated oil receiving operation, the internal flow law for internal floating roof tanks, and the impact of oil flow on floating roofs is not yet clear. Therefore, investigating the flow field features and influence characteristics of the oil flow that impacts a floating roof in the bottoming state is highly significant for the protection of floating roofs, pollution control, and area safety.

To study the process by which an oil tank with a dropped floating roof receives oil, it is necessary to simulate the two-phase flow of air and oil. The volume of fluid (VOF) multiphase flow model can be used to track the air-liquid interface and calculate the volume fraction accounted for by the two-phase flow components, and the turbulence model can be used to simulate the turbulence in the oil receiving process; there are many applications for numerical simulations in this area of research (Fang et al., 2020). Previous research has involved the use of numerical techniques to analyze the heat transfer performance of turbulent flow inside a coaxial cylinder with a complex slit surface and to explore the synergistic relationship between fluid temperature and velocity fields (Sun et al., 2023a). Further, the flow behavior and heat transfer characteristics in a coaxial cylindrical annular gap with a magnetic field have been numerically simulated by modifying the standard k-ε turbulence model, and the mechanism by which the magnetic field regulates the flow and heat transfer characteristics have been elucidated (Sun et al., 2023b). Jalili P et al. (2022) numerically simulated the mixed nanofluid flow and heat transfer processes in a discontinuous spiral baffle shell and tube heat exchanger using the finite volume method, and they also predicted the thermal performance of the spiral baffle heat exchanger using the renormalization group k-ε turbulence model to obtain the ratio of heat transfer coefficient to pressure drop. Jalili B et al. (2022) numerically simulated the turbulence and heat transfer processes in a countercurrent two-tube heat exchanger using the standard k-ε turbulence model to derive convective heat transfer characteristics. Ji et al. (2024) used Ansys Fluent software to numerically simulate the phase change processes of phase change materials in a three-tube heat exchanger via the finite volume method, and they characterized heat storage efficiency based on liquid fraction, temperature, and velocity. Furthermore, the effect of airflow turbulence intensity on the penetration and fragmentation of liquid jets has been numerically investigated using the VOF model and the large eddy simulation method (Jalili et al., 2023). The effect of humidified combustion products on the performance of a boiler exhaust gas preheater with spiral internal geometry has been numerically investigated using the finite volume method and the realizable k-ε turbulence model (Salehipour et al., 2024). Hassanvand et al. (2010) utilized the VOF model to numerically simulate the gasoline evaporation process during the splash loading of a gasoline tank and to investigate the effects of different parameter variations on gasoline losses. In addition, Hassanvand et al. (2011) studied the interphase mass transfer process in gas-liquid multiphase systems using the VOF model. Haelssig et al. (2010) used the VOF model to track the dynamic interface of a gas-liquid two-phase flow and also investigated the mass transfer law at the dynamic interface. Zhang et al. (2020) numerically simulated the oil vapor diffusion process that occurs in internal floating roof tanks using the realizable k-ε turbulence model and also investigated the effects of parameter changes such as floating roof height and ambient wind velocity on the oil vapor diffusion process within internal floating roof tanks. Research on the oil flow state in large storage tanks has primarily focused on numerical simulations of the flow and temperature fields in the tanks. Zhao et al. (2016, 2017, 2020, 2024) investigated the flow and heat transfer characteristics of the static storage and receiving and delivering processes of raw petroleum in floating roof tanks using the thermal oil injection heating method and the standard k-ε turbulence model. Further, Wang et al. (2018, 2019) utilized the standard k-ε turbulence model to numerically simulate the turbulent flow and heat transfer process of a 100,000 m^3 floating roof oil storage tank during long-term oil storage. They also investigated the associated kinetic energy, turbulent viscosity, and oil temperature evolution laws. The coupled properties of heat transmission and flow in the heating process of a raw petroleum coil were identified by Sun et al. (2018, 2023), who used a turbulence model to numerically simulate the heating process in a big floating roof tank with a steam coil.



Fig. 1. Damaged aluminum floating roof of an internal floating roof tank.

The evaporation law, the interphase mass transfer law, and the flow and heat transfer properties of the static storage, receiving, delivering, and heating processes of raw petroleum tanks were the main topics of the majority of the aforementioned studies. The flow field characteristics and influencing characteristics of the oil flow impacting the floating roof during the oil receiving process have not yet been studied. Accordingly, the focus of the present study was to analyze the oil receiving process of an internal floating roof tank under the roof bottoming condition. Ansys Fluent software and the finite volume method were used to solve partial differential equations following the discretization of the flow field; the VOF model and the realizable k-ε turbulence model were applied to establish an oil receiving model of the tank; and it was solved using the pressure implicit with splitting of operators (PISO) algorithm. The flow field characteristics and impact characteristics of the liquid striking the floating roof were analyzed and compared for

different oil inlet velocities, initial liquid levels, medium densities, and oil tank diameters. The study findings would provide the technical support and theoretical underpinnings needed to implement further safety precautions for internal floating roof tanks as well as references for the prevention and control of major hazard source accidents in safety production.

2. Experimental methods

2.1. Physical model

The object of this study was an internal floating roof tank, as shown in Fig. 2a. Only the influence of the oil flow impact on the floating roof during the oil receiving process was considered; other factors, such as the quality of the floating roof, problems with installation, uneven settlement of the tank bottom roof, corrosion of the equipment, and the influence of the production operation, were disregarded. To model the scenario and proceed with the simulation without increasing the workload of numerical calculations, the following simplifications were necessary:

(1) To enable successful modeling, the structure of the floating roof was simplified to a cylinder with a thickness of 1 mm and the same radius as the tank. Tank deformation and the sealing method were not considered, and only the flow field calculation domain below the floating roof was established.
(2) Since the present study focused on the flow field distribution of the oil, on which changes in environmental temperature and wind velocity have little influence, heat transfer was disregarded, and changes in environmental temperature and wind velocity were not considered.
(3) Volatilization of the oil was not considered.
(4) The tank inlet velocity was controlled at 2.5–4.0 m/s; the receiving oil velocity was kept constant; and four different constant flow velocities were selected for the simulation calculations.

This simplification process was carried out for a large 1000 m^3 internal floating roof tank in the field to obtain a three-dimensional physical model, as shown in Fig. 2b (Huang et al., 2019, 2020b; 2020c). In line with the principle of similarity, the model tank was obtained by scaling down the original dimensions 14 times. The model tank was used only for the experimental verification of the accuracy of the mathematical model and numerical methods. To investigate how changing the tank diameter would influence the impact characteristics of the floating roof, three kinds of internal floating roof tanks were modeled: 3000 m^3, 5000 m^3, and 10,000 m^3. The specific dimensions of the physical models are shown in Table 1.

2.2. Fluid mathematical model

2.2.1. VOF model

The flow process of the oil received in the internal floating roof tank was simulated and computed using the Eulerian multiphase flow VOF model. A common set of momentum equations are shared by the gas-liquid two-phase flow components in the VOF model, so the volume fractions occupied by these components were noted in each computing unit of the fluid computational domain throughout the calculations. The VOF model allows for tracking the interface between a gas phase and a liquid

Phase by solving the volume fraction equation (Eq. (1)).

$$\frac{\partial \alpha}{\partial t} + \boldsymbol{u} \cdot \nabla \alpha = 0 \tag{1}$$

Here, α represents the volume fraction, t is the oil flow time in seconds, $\boldsymbol{u}$ is the velocity vector of the solved phase in $m \cdot s^{-1}$, and ∇ is the Laplace operator. When a fluid domain grid is completely filled with air, $\alpha = 1$. Conversely, when a fluid domain grid is completely filled with oil, $\alpha = 0$. When a gas phase and a liquid phase coexists, $0 < \alpha < 1$.

2.2.2. Continuity equation

Any flow process must satisfy the law of conservation of mass, and the process of receiving oil in an internal floating roof tank is a flow problem. Therefore, the oil receiving process must satisfy the law of conservation of mass, which states that the net mass

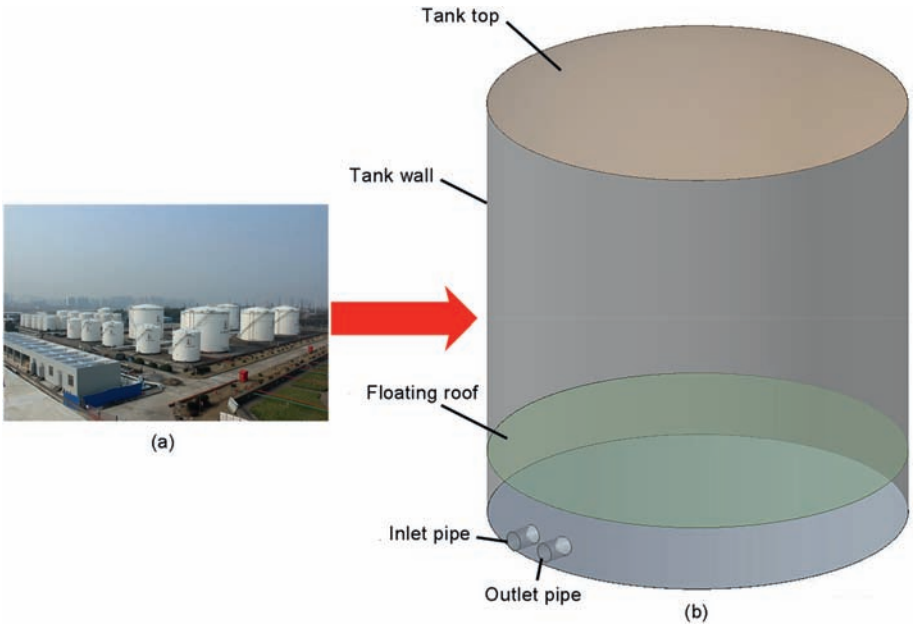


Fig. 2. The research object for the numerical simulation. (a) The on-site large internal floating roof tanks. (b) The 3D physical model.

Table 1
Internal floating roof tank specifications.

Tank capacity (m^3)	Diameter (m)	Floating roof thickness (m)	Inlet pipe Diameter (m)	Sinking disk accident state floating roof height (m)
Model tank	0.822	0.001	0.036	0.129
1000	11.5	0.001	0.5	1.8
3000	17	0.001	0.5	1.8
5000	21	0.001	0.5	1.8
10,000	28	0.001	0.5	1.8

entering an infinitesimal body during a given time period equals the mass increase per unit of time in the fluid. The oil stored in an internal floating roof tank is an incompressible fluid, and the differential form of the associated equation is as follows (Eq. (2)).

$$\frac{\partial \rho}{\partial t}+\frac{\partial(\rho u_x)}{\partial x}+\frac{\partial(\rho u_y)}{\partial y}+\frac{\partial(\rho u_z)}{\partial z}=0 \tag{2}$$

The velocity components in three directions (xyz) are each denoted by u_x, u_y, and u_z in $m\cdot s^{-1}$, and ρ is the oil density in $kg\cdot m^{-3}$.

2.2.3. Momentum equation

Any flow system, including the flow process of receiving oil in an internal floating roof tank, must satisfy the law of conservation of momentum, which states that the rate at which a fluid's momentum changes over time is equal to the sum of the forces from the outside world acting on the infinitesimal body. The following are the differential forms of the associated equations (3)–(5):

$$\begin{aligned}&\frac{\partial(\rho u_x)}{\partial t}+u_x\frac{\partial(\rho u_x)}{\partial x}+u_y\frac{\partial(\rho u_x)}{\partial y}+u_z\frac{\partial(\rho u_x)}{\partial z}\\&\quad=-\frac{\partial p}{\partial x}+\mu\left(\frac{\partial^2 u_x}{\partial x^2}+\frac{\partial^2 u_x}{\partial y^2}+\frac{\partial^2 u_x}{\partial z^2}\right)+\rho f_x\end{aligned} \tag{3}$$

$$\begin{aligned}&\frac{\partial(\rho u_y)}{\partial t}+u_x\frac{\partial(\rho u_y)}{\partial x}+u_y\frac{\partial(\rho u_y)}{\partial y}+u_z\frac{\partial(\rho u_y)}{\partial z}\\&\quad=-\frac{\partial p}{\partial y}+\mu\left(\frac{\partial^2 u_y}{\partial x^2}+\frac{\partial^2 u_y}{\partial y^2}+\frac{\partial^2 u_y}{\partial z^2}\right)+\rho f_y\end{aligned} \tag{4}$$

$$\begin{aligned}&\frac{\partial(\rho u_z)}{\partial t}+u_x\frac{\partial(\rho u_z)}{\partial x}+u_y\frac{\partial(\rho u_z)}{\partial y}+u_z\frac{\partial(\rho u_z)}{\partial z}\\&\quad=-\frac{\partial p}{\partial z}+\mu\left(\frac{\partial^2 u_z}{\partial x^2}+\frac{\partial^2 u_z}{\partial y^2}+\frac{\partial^2 u_z}{\partial z^2}\right)+\rho f_z\end{aligned} \tag{5}$$

The unit mass force components in three directions are represented by f_x, f_y, and f_z in $m\cdot s^{-2}$; t is the oil flow time in s; p is the oil absolute pressure in Pa; μ is the oil dynamic viscosity in $kg\cdot(m\cdot s)^{-1}$; and g represents the oil gravity acceleration in $m\cdot s^{-2}$.

2.2.4. Turbulence equation

When an internal floating roof tank receives oil products, fluid particles are affected by impact and mixing and exhibit unstable flow and turbulence. Therefore, to ensure the reliability of numerical calculation results, it is necessary to choose a suitable turbulence model for simulation. The realizable k-ε model is a simple, computationally stable, and computationally efficient model that can save computation time and meet accuracy requirements and is thus widely used in turbulence simulations in engineering (Wang, 2004). The turbulent kinetic energy transport equation for incompressible fluid is given below (Eq. (6)):

$$\begin{aligned}&\frac{\partial(\rho k)}{\partial t}+\frac{\partial(\rho k u_x)}{\partial x}+\frac{\partial(\rho k u_y)}{\partial y}+\frac{\partial(\rho k u_z)}{\partial z}\\&\quad=\frac{\partial}{\partial x}\left[\left(\mu+\frac{\mu_t}{\sigma_k}\right)\frac{\partial k}{\partial x}\right]+\frac{\partial}{\partial y}\left[\left(\mu+\frac{\mu_t}{\sigma_k}\right)\frac{\partial k}{\partial y}\right]\\&\quad+\frac{\partial}{\partial z}\left[\left(\mu+\frac{\mu_t}{\sigma_k}\right)\frac{\partial k}{\partial z}\right]+G_k+G_b-\rho\varepsilon-Y_M+S_k\end{aligned} \tag{6}$$

The transport equation for the incompressible fluid dissipation rate is given below (Eq. (7)).

$$\begin{aligned}&\frac{\partial(\rho\varepsilon)}{\partial t}+\frac{\partial(\rho\varepsilon u_x)}{\partial x}+\frac{\partial(\rho\varepsilon u_y)}{\partial y}+\frac{\partial(\rho\varepsilon u_z)}{\partial z}\\&\quad=\frac{\partial}{\partial x}\left[\left(\mu+\frac{\mu_t}{\sigma_\varepsilon}\right)\frac{\partial \varepsilon}{\partial x}\right]+\frac{\partial}{\partial y}\left[\left(\mu+\frac{\mu_t}{\sigma_\varepsilon}\right)\frac{\partial \varepsilon}{\partial y}\right]\\&\quad+\frac{\partial}{\partial z}\left[\left(\mu+\frac{\mu_t}{\sigma_\varepsilon}\right)\frac{\partial \varepsilon}{\partial z}\right]+\rho C_1 S\varepsilon\\&\quad-\rho C_2\frac{\varepsilon^2}{k+\sqrt{\upsilon\varepsilon}}+C_{1\varepsilon}\frac{\varepsilon}{k}C_{3\varepsilon}G_b+S_\varepsilon\end{aligned} \tag{7}$$

Here, S, S_k, and S_ε are customized source items; k is the turbulent kinetic energy; ε is the dissipation rate; μ_t is the turbulent viscosity; υ is the kinematic viscosity in $m^2\cdot s^{-1}$; G_k denotes the turbulent kinetic energy due to the mean velocity gradient; G_b denotes the turbulent kinetic energy due to buoyancy (for incompressible fluids, $G_b=0$); Y_M denotes the contribution of pulsating expansion to the overall dissipation rate in a compressible flow (for incompressible fluids, $Y_M=0$); σ_k and σ_ε are the Prandtl numbers corresponding to the turbulent kinetic energy k and dissipation rate ε, respectively, and are empirical values; and C_1, C_2, $C_{1\varepsilon}$ and $C_{3\varepsilon}$ are empirical constants (when the shear flow direction is the same as the gravitational direction, $C_{3\varepsilon}=1$; when the shear flow is perpendicular to the gravity direction, $C_{3\varepsilon}=0$).

2.3. Physical properties of oil

To investigate the flow properties of the oil impacting the floating roof in the present study, four light oils with different densities, namely naphtha, gasoline, kerosene, and diesel, were selected as storage media. Table 2 displays the physical property data for each oil. Each oil's density was measured using a petroleum densitometer, and kinematic viscosity was measured using a

Table 2
The physical properties of oils and solids used in the calculation process.

Oil type	Density (kg/m^3)	Dynamic viscosity [$kg/(m\cdot s)$]
Naphtha	690	0.0004
Gasoline	728	0.0006
Kerosene	780	0.0012
Diesel	835	0.0042

kinematic viscometer. Dynamic viscosity was then calculated according to Equation (8).

$$\mu = \rho v \tag{8}$$

2.4. Initial condition and boundary condition

Air was the main phase, and oil was the second phase in the fluid domain. The inlet set to the velocity inlet, and different liquid levels were used as initial conditions for the simulation. Considering that the function of a venting valve is to regulate pressure, the pressure outlet was at the position of the venting valve. Based on the actual oil receiving and delivering velocities at the oil depot, as well as the liquid level requirements and tank volume, the initial liquid levels were set at 0.5 m, 1.0 m, and 1.5 m; the inlet velocities were 2.5 m/s, 3.0 m/s, 3.5 m/s, and 4.0 m/s; the tank diameters were 11.5 m, 17 m, 21 m, and 28 m; the inlet and outlet gauge pressures were 0; the inlet and outlet turbulence intensity was 5%; and turbulence viscosity was set at 10.

2.5. Grid independence analysis

To eliminate any errors arising from mesh quality and quantity in the calculation results, mesh independence validation was conducted to determine the mesh size that would allow for reliable calculation accuracy and the least consumption of computational resources and time. The structured meshing of the fluid domain (see Fig. 2b) was performed using Ansys Meshing software, and the velocity inlet and the region near the inlet were encrypted, as shown in Fig. 3a–c. By reducing the length of the cell size, the number of the four computational grids were 89,136, 132,365, 233,854, and 357,640, respectively, and the grid quality was found to meet the requirements in Table 3. The findings of the grid independence analysis (see Fig. 3d) showed that when the number of grids reached 132,365, 233,854, and 357,640, the corresponding maximum pressure values of the floating roof subjected to the liquid impact did not change much, while the maximum pressure value of the grid number 89136 was larger than the value of all the above three grids, so 132,365 grids were used for the numerical calculations in this study. The quality of this mesh and the generated grid met the computational requirements; the results are shown in Table 3. The grid division method used for 1000 m^3 tank was also used for the model tank and the 3000 m^3, 5000 m^3, and 10,000 m^3 internal floating roof tanks, and the grid irrelevance analysis method was also similar, so the explanations are not repeated here.

2.6. Numerical method

The flow field in the fluid domain was simulated using the Ansys Fluent 2022R1 solver. The nonlinear partial differential equations were converted into linear algebraic equations on the grid cells

Table 3
Grid quality of fluid domain.

Evaluation parameter	Requirement	Numerical value
Element quality	$Q_{EQ(avg)} \geq 0.75$	0.86
Aspect ratio	$0 \leq Q_{AR(max)} \leq 35$	15
Skewness	$0 \leq Q_{S(max)} \leq 0.95$	0.50
Orthogonal quality	$Q_{OQ(min)} \geq 0.10$	0.73

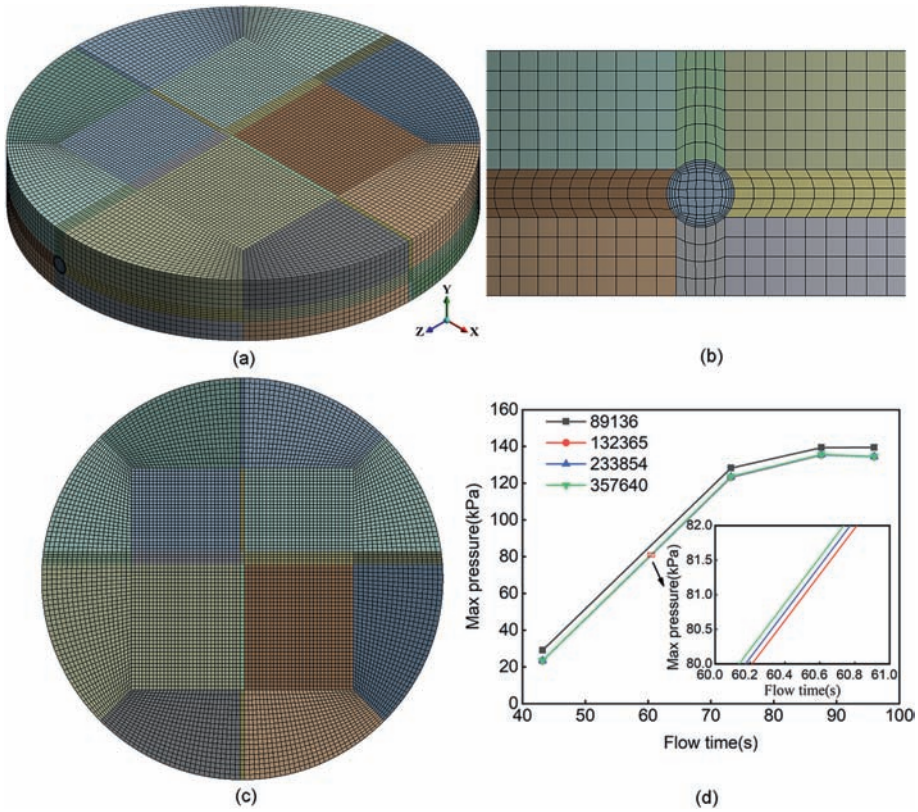


Fig. 3. Structured mesh generation and grid independence analysis. (a) Fluid domain grid. (b) Inlet grid boundary layer encryption. (c) Flow-solid coupling surface grid. (d) Grid independence analysis.

using the finite volume method, and the flow field solution was obtained by solving the linear system of equations. A solver based on the pressure method was chosen to use the absolute velocity required to solve the velocity equation. For computing transient problems, the pressure-velocity coupled PISO (Issa, 1986; Oliveira and Issa, 2001) algorithm, which is computationally faster and has more accurate data compared to couple's algorithm, was chosen. For spatial discretization, the second-order windward format was selected, and for time term discretization, the first-order implicit format was selected. The tank level was determined based on level meter readings. The numerical calculation process is shown in Fig. 4.

2.7. Experimental test

A set of small-scale experimental internal floating roof tank systems involving oil receiving and delivering processes was constructed (see Fig. 5a) to investigate the impact characteristics of oil flow against floating roofs. The results of the numerical simulation were verified experimentally to determine the feasibility of the mathematical model and numerical calculation method. At a pump speed of 1450 r/min, the flow rate size was controlled by adjusting the inlet valve opening and the flow meter reading. To test the pressure at which the oil flow impacted the floating roof during the oil receiving process, five pressure test sites were set up on the floating roof (see Fig. 5b). A pressure sensor was used to gather the pressure values from T_1 to T_5. The findings of the numerical simulation and the experimental pressure measurements at five locations on the floating roof (T_1–T_5) are displayed in Fig. 6. The overall change trends were consistent between the two sets of findings, which indicated that the construction of the model, the parameter settings for the numerical simulation, and the selection of numerical methods were reasonable. Therefore, numerical predictions of the flow field characteristics and force conditions of oil flow impacting the large internal floating roof tanks could be made.

3. Results and discussion

3.1. Analysis of the time course response of the maximum pressure of the floating roof impacted by liquid under different working conditions

To determine the maximum degree of effect of the oil flow impacting the floating roof under four different working conditions, a liquid impact maximum pressure over time curve (Fig. 7) was generated. When the floating roof was down to 1.8 m (floating roof at the bottom), with different oil inlet velocities, initial liquid levels, media densities, and tank diameters across the four operational conditions, the maximum pressure of liquid impact on the floating roof all varies with over time, and the trend was consistent under the same type of operating conditions (Teng et al., 2021). During the initial stage of the oil receiving process, as the oil level rose, the oil exerted pressure on the gas between the liquid level and the floating roof, and, in turn, the gas exerted pressure on the floating roof, but the increase in pressure at this stage was not large. The maximum pressure then began to rise rapidly, and the impact of the oil flow on the floating roof increased suddenly. In the middle and late stages of the oil receiving process, the maximum pressure

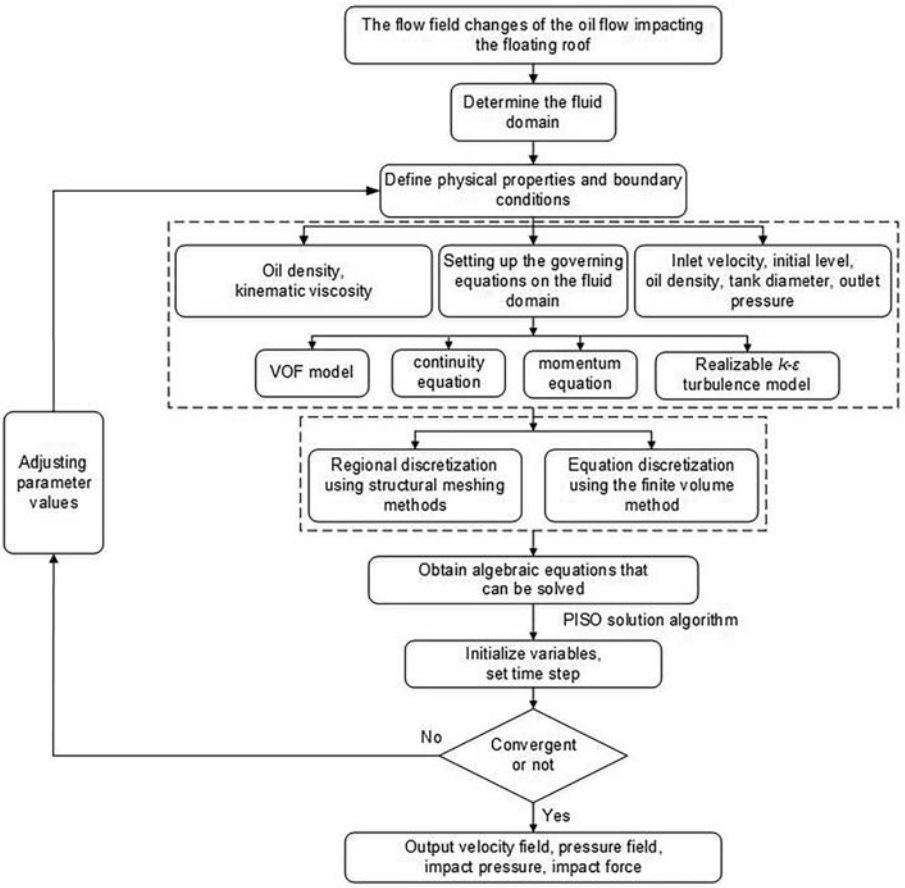


Fig. 4. Numerical calculation flowchart.

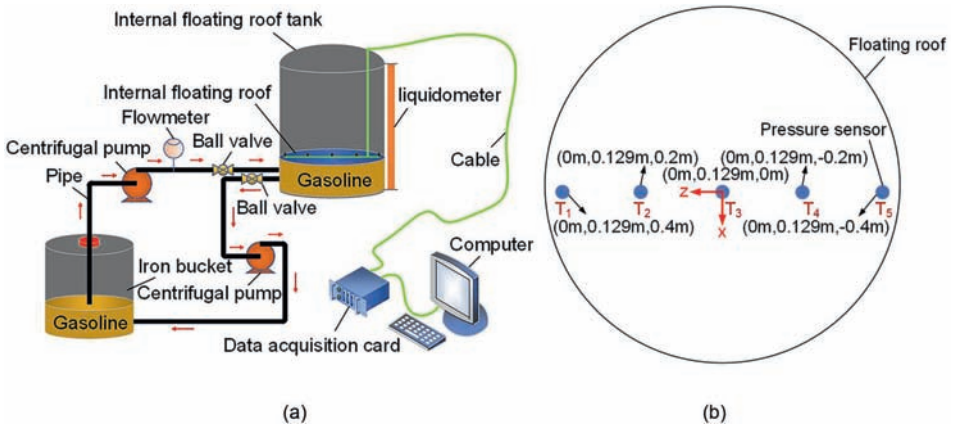


Fig. 5. The experimental system for the oil receiving and delivering process. (a) Experimental setup. (b)The distribution of pressure test points on the floating roof.

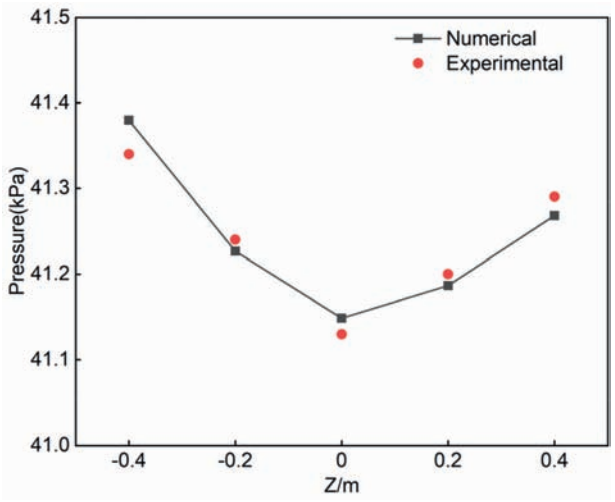


Fig. 6. Comparison of the simulated and experimental pressure values for the oil flow impacting the floating roof.

continues to rise until it reaches its maximum value throughout impact process. The pressure finally stabilized until the tank filled up. As shown in Fig. 7a, the oil inlet velocities of 2.5 m/s, 3.0 m/s, 3.5 m/s, and 4.0 m/s corresponded to the maximum pressure peak values of 53.159 kPa, 76.1 kPa, 103.6 kPa, and 135.5 kPa, respectively; thus, as the oil inlet velocity increased, the increase in maximum pressure was very large. This can be explained by the momentum theorem, according to which, at the same medium density, the higher the oil inlet velocity, the greater the impact force of the oil flow on the floating roof and the higher the pressure. This suggests that the changes in oil inlet velocity greatly affected the oil's impact on the floating roof. The higher the oil inlet velocity, the bigger the impact and the more unfavorable the conditions for the protection of the floating roof. Accordingly, in engineering, low oil inlet velocities should be used for oil receiving operations. As shown in Fig. 7b, the peak pressure values of 135.81 kPa, 135.79 kPa, and 135.63 kPa corresponded to the initial liquid levels of 0.5 m, 1.0 m, and 1.5 m, respectively. This means that the maximum pressure changed very little as the initial liquid level increased, indicating that changes in the initial liquid level had little influence on the liquid's impact on the floating roof. From Fig. 7c, it can be seen that the maximum pressure peaks for naphtha, gasoline, kerosene, and diesel were 128.5 kPa, 135.5 kPa, 144.9 kPa, and 154.9 kPa, respectively, indicating that the maximum pressure was higher for higher medium densities. According to the momentum theorem, at the same oil inlet velocity, the higher the density of the medium, the greater the impact force of the oil flow on the floating roof and the higher the pressure. This indicates that changes in the density of the medium on the floating roof by the liquid impact of the larger influence, the greater the density of the medium, the greater the impact effect. Therefore, when storing a high-density light oil for oil receiving operations, attention should be paid to the protection of the floating roof. As shown in Fig. 7d, the 1000 m^3, 3000 m^3, 5000 m^3, and 10,000 m^3 tank volumes corresponded to the maximum pressure peaks of 135.5 kPa, 134.1 kPa, 133.5 kPa, and 133.33 kPa, respectively. Thus, the maximum pressure was lower for higher tank diameters. This is because the smaller the diameter of a storage tank, the more concentrated the impact of the oil flow on the floating roof due to the limited space, and the overall pressure level is relatively high. At a constant oil inlet velocity, the energy of the oil flow is distributed over a smaller floating roof area, resulting in a higher pressure per unit area. This shows that changes in the tank diameter influence the impact of the oil on the floating roof; the bigger the diameter of the tank, the smaller the impact of the oil, which is more conducive to the protection of the floating roof.

3.2. Pressure distribution on the floating roof impacted by liquid under different working conditions

To determine the features of the pressure field on the surface of a floating roof impacted by oil in the bottoming state, a cloud diagram of the pressure distribution at the moments of maximum pressure under the four different working conditions was created. Fig. 8a shows that at oil inlet velocities of 2.5 m/s and 3.0 m/s, the pressure in the floating roof area above the inlet both adjacent to and opposite the inlet was higher. The central area of the floating roof was mainly affected by the static pressure of the oil product and less affected by the impact, resulting in no significant pressure fluctuations. At an oil inlet velocity of 3.5 m/s, the pressure by the edge of the floating roof increased due to the influence of the tank wall constraints and oil flow rebound. At an oil inlet velocity of 4.0 m/s, the pressure fluctuation in the floating roof area above the opposite side of the inlet was frequent and intense, and a strong-impact high-pressure zone appeared due to the interaction between the high-velocity oil flow and the tank wall. At an oil inlet

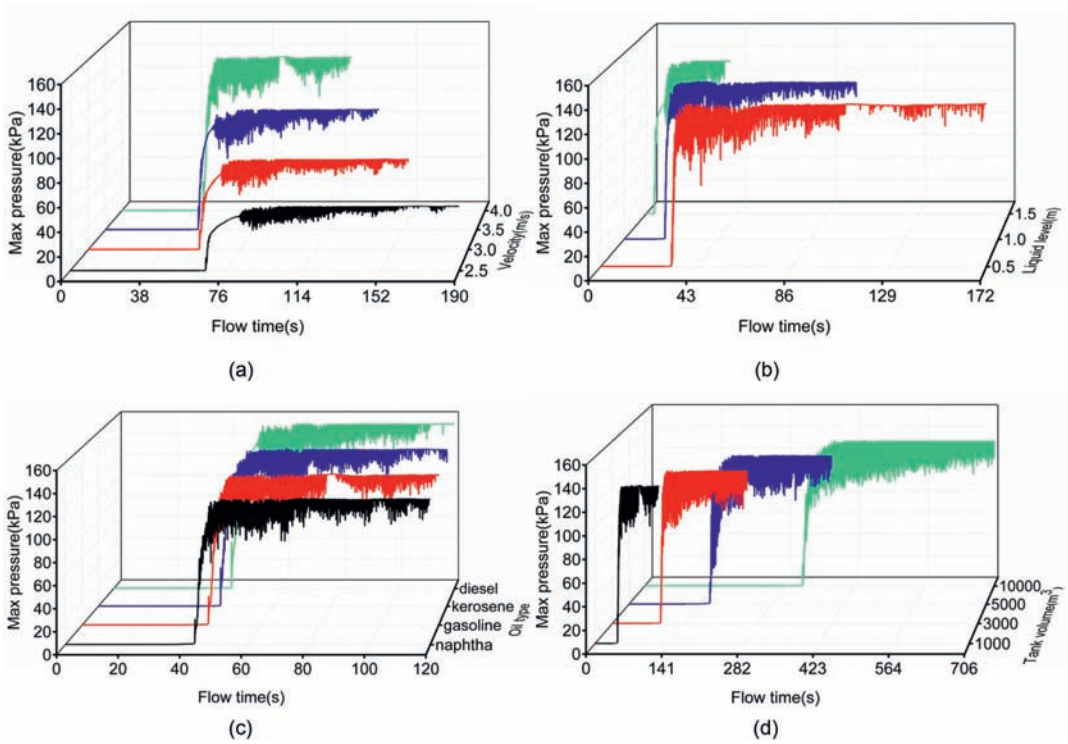


Fig. 7. Time response of the maximum pressure of a floating roof subjected to liquid impact under four different operating conditions. (a) Different oil inlet velocities. (b) Different initial liquid levels. (c) Different medium densities. (d) Different tank diameters.

velocity of 2.5 m/s, the maximum pressure zone on the surface of the floating roof was in the upper area opposite the inlet, and the area was very small. At an oil inlet velocity of 3.0 m/s, the maximum pressure zone was at the left corner edge of the floating roof, situated the upper area opposite the inlet, and an increased area compared to an oil inlet velocity of 2.5 m/s. At 3.5 m/s, the maximum pressure zone was at the edge of the floating roof to the right of the inlet axis, as well as at three scattered locations. At 4.0 m/s, the maximum pressure zone was at the left corner of the floating roof, situated the upper area opposite the inlet. All of the abovementioned maximum pressure zones should be considered the key protection areas for floating roofs during daily oil receiving processes (Huang et al., 2020a).

As shown in Fig. 8b, the floating roof regions above the inlet on the same side and on the opposite side were the high pressure regions associated with different initial liquid levels. As the initial liquid level increased, the pressure distribution of the floating roof changed due to the buffering effect of the oil flow. When the initial liquid level was 0.5 m, the maximum pressure zone was at the left corner of the floating roof, situated the upper part of opposite the inlet. When the initial level was 1.0 m, the maximum pressure zone was at the upper edge of the floating roof, situated opposite the inlet. When the initial liquid level was 1.5 m, the maximum pressure zone was at the upper left corner of the floating roof, situated opposite the inlet. Thus, the left corner and the edge of a floating roof, both the upper area opposite the inlet, are the key locations requiring protection during the oil receiving process.

As shown in Fig. 8c, the floating roof region opposite the inlet was the high pressure zone when different densities of oil were received. When naphtha was the medium, the maximum pressure zone was at the left corner of the floating roof, situated the upper area opposite the inlet. When gasoline was the medium, the maximum pressure zone was at the edge of the floating roof, situated the upper area opposite the inlet. When kerosene was the medium, the maximum pressure zone was at the lower left corner of the floating roof in the upper area opposite the inlet. When diesel was the medium, the maximum pressure zone was at the lower left corner of the floating roof, situated the upper area opposite the inlet. The left corner, the lower left corner, and the edge of the floating roof in the upper area opposite the inlet are the key areas for protection during oil receiving operations.

As shown in Fig. 8d, when the volume of the tank was 1000 m^3, the maximum pressure zone was at the edge of the floating roof, situated the upper area opposite the inlet, and had a relatively small area. When the volume of the tank was 3000 m^3, the maximum pressure zone was at the lower left corner of the floating roof, situated the upper area opposite the inlet, and an increased area compared to the tank volume of 1000 m^3. When the volume of the tank was 5000 m^3, the maximum pressure zone was dispersed at the lower left corner of the floating roof, situated the upper area opposite the inlet, and the area continued to grow. When the volume of the tank was 10,000 m^3, the maximum pressure zone was dispersed at the edge of the floating roof above the inlet on both sides and in the left red area of the float roof in the upper area opposite the inlet, and the area continued to increase. This was because the tank's large diameter provided a wide space for the oil to flow and quickly spread around, and the energy was dispersed in a large area of the floating roof, resulting in a large maximum pressure area.

3.3. Flow field distribution on the floating roof impacted by liquid under different working conditions

To understand the distribution of the flow field during the oil receiving process when a floating roof is in the bottoming state, the characteristics and distribution of the flow lines under four different conditions at moments of maximum impact pressure were analyzed and compared. As shown in the 3D streamline diagram in Fig. 9, when receiving oil products under four different operating

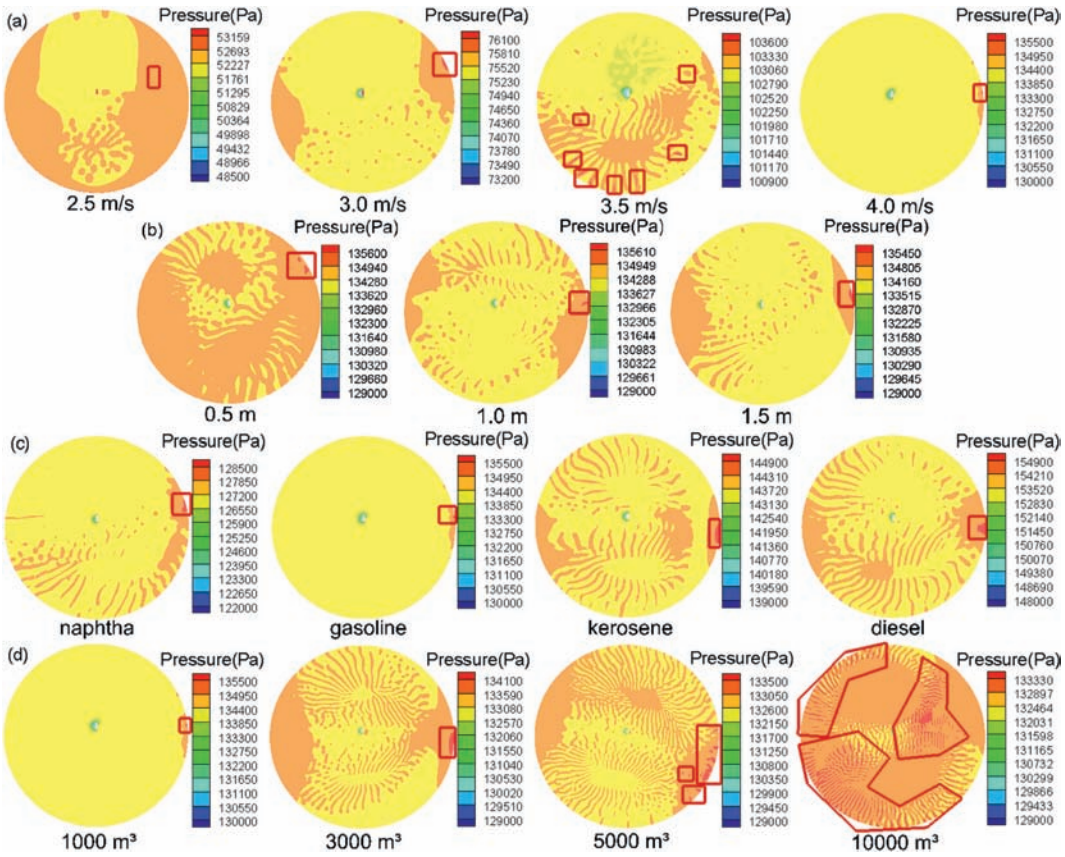


Fig. 8. Cloud diagram of the floating roof pressure distribution at moments of maximum pressure on a floating roof impacted by liquid under four different working conditions. (a) Different oil inlet velocities. (b) Different initial liquid levels. (c) Different medium densities. (d) Different tank diameters.

conditions—that is, different oil inlet velocities, initial liquid levels, medium densities, and tank diameters—vortices appeared below the liquid level as the liquid level increased, likely due to continuous extrusion and agitation of the fluid, resulting in a turbulent flow (Huang et al., 2016). The oil flow was distributed along both sides of the inlet axis, and the rotational direction of the vortex was counterclockwise along the left side of the inlet axis and clockwise along the right side of the inlet axis. The oil flowed from the inlet to the tank wall on the opposite side and then divided into two parts. One part moved up toward the floating roof, and the other part reached the tank wall opposite the inlet and flowed along it toward the inlet, subsequently meeting the filled level of oil; thus, two vortices were formed symmetrically on both sides of the inlet. The vortices rotated counterclockwise along the left side of the inlet axis and clockwise along the right side of the inlet axis. As shown in the Y-Z cross-section flow line diagram in Fig. 9a, an oil inlet velocity of 2.5 m/s led to a small vortex that was mainly distributed at the upper end of the inlet. At an oil inlet velocity of 3.0 m/s, a small vortex that rotated clockwise appeared at the bottom of the tank, opposite the inlet. At 3.5 m/s, a small vortex that rotated counterclockwise appeared close to the floating disc opposite the inlet. At a 4.0 m/s oil inlet velocity, small vortices were formed at the inlet's upper and lower ends, and a large vortex that rotated clockwise appeared at the bottom of the tank on the opposite side of the inlet. These observations indicate that as the oil inlet velocity increased, the more turbulent the oil flow near the inlet and near the opposite the inlet. As shown in the Y-Z cross-sectional streamline diagram in Fig. 9b, when considering initial liquid levels of 0.5 m and 1.0 m, the oil flow disturbance at the inlet's upper and lower ends was greater at 0.5 m than at 1.0 m. At the same time, there was a large clockwise rotating vortex at the bottom of the tank, opposite the inlet. When the initial liquid level was 1.5 m during the oil receiving process, a small vortex was observed at the upper end of the inlet, along with a small counterclockwise-rotating vortex near the floating roof on the side opposite the inlet. As shown in the Y-Z cross-sectional streamline diagram in Fig. 9c, when naphtha was the medium, a little vortex that rotated clockwise appeared at the bottom of the tank, on the side opposite the inlet. When gasoline was the medium, the flow field distribution law was the same for both oil streams, as the conditions were the same as those in the simulation involving the 4.0 m/s inlet velocity. When kerosene was the medium, there was a large counterclockwise-rotating vortex located close to the floating roof on the side opposite the inlet. When diesel was the medium, there was a small vortex rotating clockwise at the bottom of the tank on the side opposite the inlet. The oil flowed from the inlet to the tank wall on the opposite side and then divided into two. One part directly hit the floating roof, and the impact force increased, while the other part formed a small vortex that rotated clockwise at the bottom of the tank. As the density of the medium increased, the viscosity and flow resistance increased, and the energy diffusion of the oil flow slowed down; it was thus easy for gradients of high pressure and velocity to be formed in local areas, resulting in strong turbulence and greater impact force on the floating roof. As shown in the Y-Z cross-section flow line diagram in Fig. 9d, when the tank volume was 1000 m^3, the results were the same as those seen in the simulation condition involving a 4.0 m/s oil inlet velocity, and the flow field distribution law governing the two oil streams was the same. When the tank volume was 3000 m^3, a small vortex that rotated counterclockwise appeared immediately adjacent to the floating roof on the side opposite the inlet. When the volume of the

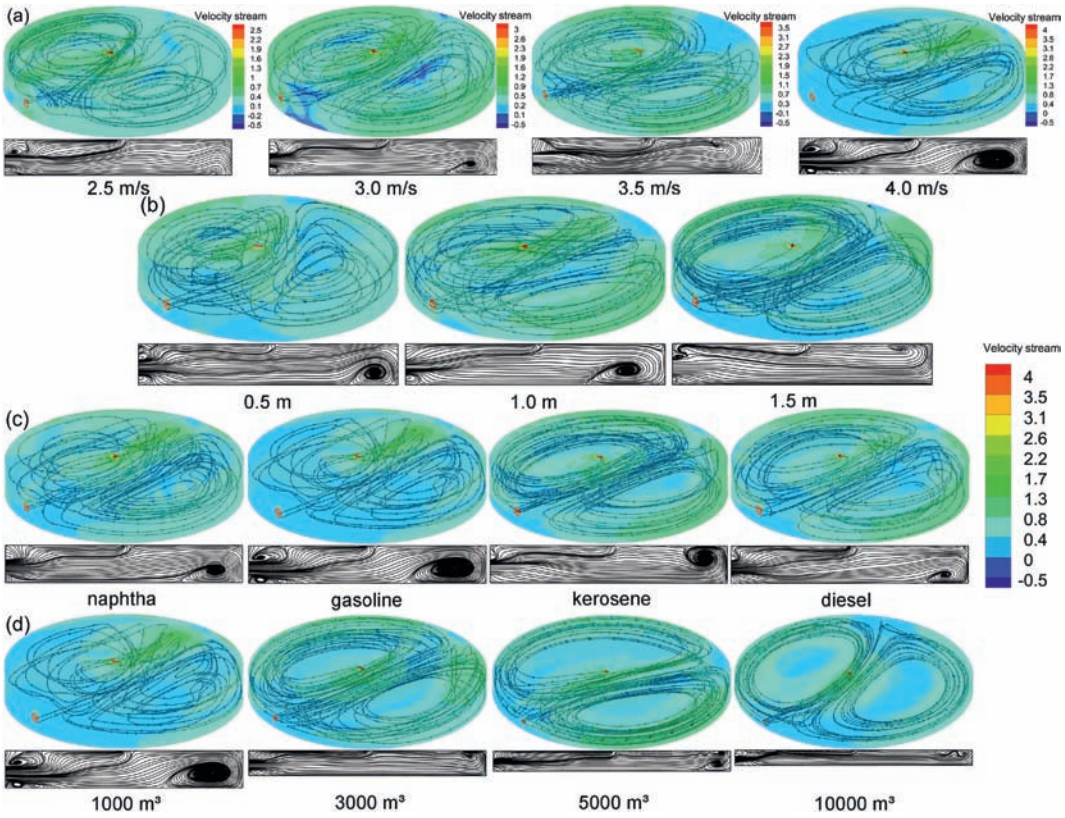


Fig. 9. Flow line distribution at the moments of the maximum pressure on the floating roof under four different working conditions. (a) Different inlet velocities. (b) Different initial liquid levels. (c) Different medium densities. (d) Different tank diameters.

storage tank was 5000 m^3, there was a little vortex rotating clockwise at the bottom of the tank on the side opposite the inlet; there was also a small vortex rotating counterclockwise near the floating roof on the side opposite the inlet, and the oil flow near the lower part of the floating roof was disturbed. When the tank volume was 10,000 m^3, the flow disturbance near the lower part of the floating roof on the side opposite the inlet increased. The findings indicate that when oil is flowing into a large-diameter tank, it takes a certain amount of time and distance for turbulence to fully develop. With the increased oil intake and continuous spreading of the oil flow, the impact pressure of the oil flow on the floating roof became relatively weak.

3.4. Analysis of the time course response of impact force on the floating roof under different working conditions

The impact force generated by the oil flow on the floating roof was the basis for measuring the degree of damage caused to the floating roof. The curves of the impact force of the liquid on the floating roof over time under four different working conditions (Fig. 10) show that the trend over time was basically the same for the different oil inlet velocities, initial liquid levels, medium densities, and tank diameters when the floating roof was in the bottom state (Teng et al., 2021). In the initial stage of oil intake, the increase in impact force was not significant, and then the impact force suddenly increased. In the middle and later stages, the impact force increased, reached its maximum value, and finally stabilized.

As shown in Fig. 10a, the impact force peaks corresponding to the oil inlet velocities of 2.5 m/s, 3.0 m/s, 3.5 m/s, and 4.0 m/s were 5.471 MN, 7.866 MN, 10.712 MN, and 13.967 MN, respectively, indicating that the impact force increased significantly as the oil inlet velocity increased. This can be explained by the momentum theorem, according to which, at the same medium density, the greater the oil inlet velocity, the greater the impact force of the oil flow on the floating roof. The impact force that the floating roof bears is greatly affected by changes in oil inlet velocity. The higher the oil inlet velocity, the more likely the floating roof is to undergo fatigue deformation or structural damage. Therefore, to protect floating roofs, it is recommended that a low velocity be used for oil receiving operations.

As shown in Fig. 10b, the impact force peaks corresponding to the initial liquid levels of 0.5 m, 1.0 m, and 1.5 m were 14.021 MN, 13.998 MN, and 13.98 MN, respectively, indicating that the impact force varied very little when the initial liquid level rose and that changes in the initial liquid level did not greatly influence the impact force endured by the floating roof. As shown in Fig. 10c, the impact force peaks corresponding to naphtha, gasoline, kerosene, and diesel were 13.251 MN, 13.967 MN, 14.97 MN, and 15.999 MN, respectively, indicating that the impact force rose noticeably as the medium density increased. According to the momentum theorem, when the oil inlet velocity remains the same, the higher the density of the medium, the greater the impact force of the oil flow on the floating roof. A change in medium density has a significant impact on the impact force borne by the floating roof. The higher the medium density, the more likely the floating roof is get deformed or be damaged. Therefore, in engineering, attention should be paid to the impact of high-density light oil on floating roofs.

As shown in Fig. 10d, the impact force peaks corresponding to the tank volumes of 1000 m^3, 3000 m^3, 5000 m^3, and 10,000 m^3 were 13.967 MN, 30.323 MN, 46.167 MN, and 81.978 MN, respectively, indicating that the impact force increased noticeably as the tank diameter increased. Thus, changes in tank diameter

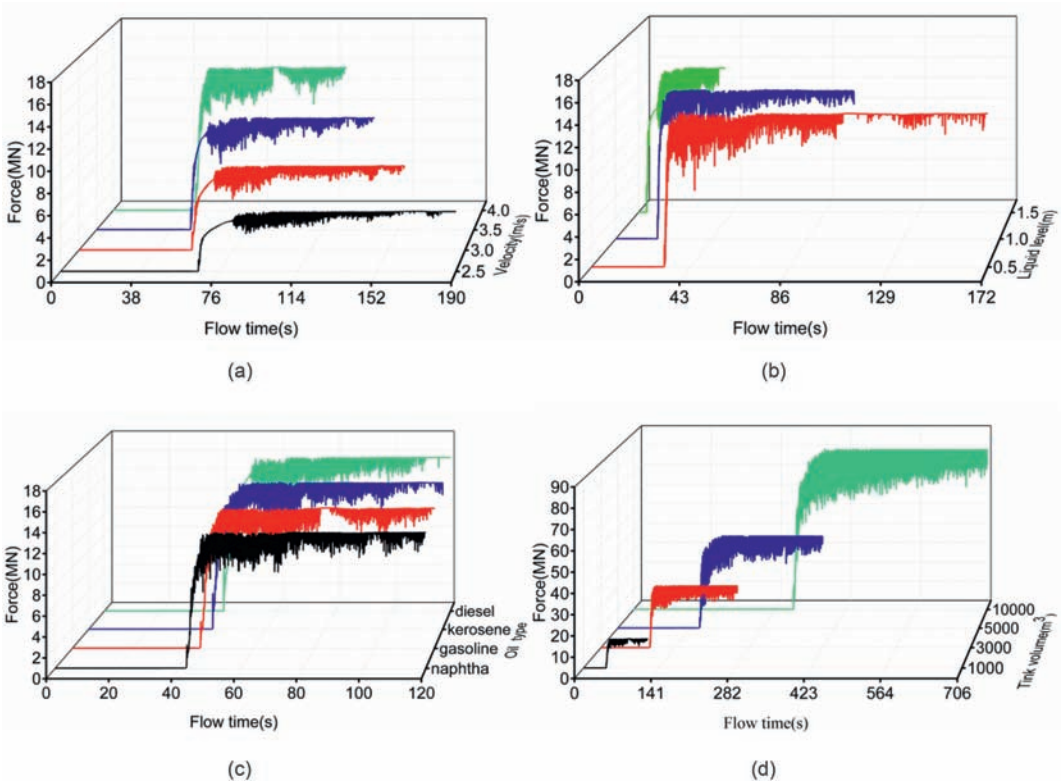


Fig. 10. Time-range responses of the impact force on the floating roof under four different operating conditions. (a) Different inlet velocities. (b) Different initial liquid levels. (c) Different medium densities. (d) Different tank diameters.

significantly affected the impact force borne by the floating roof. According to the momentum theorem, the larger the tank diameter, the greater the quality of the oil, resulting in a greater impact force.

4. Conclusion

The continuity equation, momentum equation, and turbulence equation were comprehensively calculated using Ansys Fluent, and experimental data were used to verify the feasibility of the model. Four working conditions—that is, different oil inlet velocities, initial liquid levels, medium densities, and tank diameters—were considered to research the impact characteristics of liquid on the floating roof of an internal floating roof tank during the oil receiving process in the floating roof bottoming state. The following conclusions have been drawn from the numerical results:

(1) As the oil inlet velocity increased, the maximum pressure and impact force on the floating roof increased significantly. A maximum pressure of 135.5 kPa and a maximum impact force peak of 13.967 MN were observed. These can be attributed to the increase in kinetic energy caused by the high-velocity oil inlet, which enhanced the impact action of the oil on the floating roof. Increasing the density of the medium also led to an increase in the maximum pressure and impact force on the floating roof. The associated maximum pressure was 154.9 kPa, and the highest impact force peak was 15.999 MN. Changes in the initial oil level had little effect on the impact on the floating roof; the maximum pressure was 135.81 kPa, and the impact force peak was 14.021 MN. As the diameter of the tank increased, the maximum pressure that affected the floating roof reduced, but the impact force increased. The maximum pressure was 135.5 kPa, and the highest impact force peak was 81.978 MN. As the diameter of the tank increased, the liquid distribution range became wider, and the pressure distribution was uniform, but the impact force increased due to the increase in liquid volume.

(2) As the inlet velocity increased, the more turbulent the motion on the opposite the inlet and the higher the pressure at the edge of the floating roof in the upper area of opposite the inlet. This indicates that a high-velocity oil inlet enhanced the local turbulence and, in turn, increased the force on the edge of the floating roof. Although changes in the initial liquid level had little effect on the liquid's impact on the floating roof, there was still a high-pressure zone at the edge of the floating roof in the upper area opposite the inlet, and this requires enhanced safety protection. As the density of the medium increased, the turbulent motion on the side opposite the inlet grew stronger, and the pressure at the edge of the floating roof in the upper area opposite the inlet increased. Further, as the diameter of the storage tank increased, the turbulent motion on the side opposite the inlet slowed down, but the maximum pressure zone on the floating roof became larger, indicating that the liquid's impact was distributed over a large range.

(3) To protect floating roofs, it is recommended that a low velocity, a low-density light oil, and an internal floating roof tank with a small diameter be chosen for oil receiving operations in engineering. Turbulence tends to arise opposite the inlet in an inner floating roof storage tank, with the maximum pressure distributed along the edge of the floating roof on side opposite the inlet. Therefore, increased safety precautions are needed at the edge of the floating roof to ensure that it can cope with the impact of localized high pressure and turbulence.

A simplified model was used in this study; however, in practice, other influencing factors, such as floating roof columns and sealing devices, may exist. Therefore, floating roof columns and sealing devices should be included in future research to analyze the impact characteristics of oil flow on floating roofs.

CRediT authorship contribution statement

Yan Li: Writing – review & editing, Writing – original draft. **Chunqiang Zhu:** Data curation. **Fulin Yang:** Methodology. **Xinpeng Wang:** Data curation. **Jieyao Jia:** Supervision.

Disclosure statement

The authors declare that the publishing of this work does not present any conflicts of interest.

Declaration of competing interest

The authors declare that they have no known competing financial interests or personal relationships that could have appeared to influence the work reported in this paper.

Acknowledgments

This research was supported by the Guangxi Natural Science Foundation, China (Grant No. 2022GXNSFBA035571), the Qinzhou Scientific Research and Technology Development Program Project, China (Grant No. 20233211), the Guangxi Science and Technology Major Project, China (Grant No. AA23062016-4), and the National Natural Science Foundation of China (Grant No. 22268001).

References

Adekitan, A.I., Rock, M., 2022. Lightning strike probability and current simulation for simple structures and floating roof tank. Alex. Eng. J. 61, 1643–1653.

Burmana, A.D., Benguerba, Y., Hasibuan, R., Aprilia, S., Ansari, W.R., Nova, S., Hasibuan, D.R., 2024. Investigating the catastrophic roof failure of a fatty acid storage tank: causes, mechanisms, and safety implications. J. Loss Prev. Process. Ind. 92, 105484.

Fang, J., Huang, W., Huang, F., Fu, L., Zhang, G., 2020. Investigation of the superposition effect of oil vapor leakage and diffusion from external floating-roof tanks using CFD numerical simulations and wind-tunnel experiments. Processes 8, 299.

Haelssig, J.B., Tremblay, A.Y., Thibault, J., Etemad, S.G., 2010. Direct numerical simulation of interphase heat and mass transfer in multicomponent vapour–liquid flows. Int. J. Heat Mass Tran. 53, 3947–3960.

Hassanvand, A., Hashemabadi, S.H., 2011. Direct numerical simulation of interphasemass transfer in gas–liquid multiphase systems. Int. Commun. Heat Mass Tran. 38, 943–950.

Hassanvand, A., Hashemabadi, S.H., Bayat, M., 2010. Evaluation of gasoline evaporation during the tank splash loading by CFD techniques. Int. Commun. Heat Mass Tran. 37, 907–913.

Huang, W., Wang, Z., Ji, H., Zhao, C., Lu, A., Xu, X., Wang, Y., 2016. Experimental determination and numerical simulation of vapor diffusion and emission in loading gasoline into tank. CIE J. 67, 4994–5005.

Huang, W., Fang, J., Li, F., Ji, H., Wang, H., 2019. Numerical simulation and applications of equivalent film thickness in oil evaporation loss evaluation of internal floating-roof tank. Process Saf. Environ. Prot. 129, 74–88.

Huang, W., Chen, F., Lyu, C., Zhang, G., Huang, F.Y., 2020a. Numerical simulation of oil vapor leakage and diffusion from inner floating roof tank based on wind tunnel platform experiment. Oil Gas Storage Transp. 39, 425–433.

Huang, W., Huang, F., Fang, J., Fu, L., 2020b. A calculation method for the numerical simulation of oil products evaporation and vapor diffusion in an internal floating-roof tank under the unsteady operating state. J. Pet. Sci. Eng. 188, 106867.

Huang, W., Xu, M., Li, F., Ji, H., Fang, J., 2020c. Influence of wind deviation angle on n-Hexane evaporation loss of internal floating-roof tanks. China pet. Process. Petrochem. Technol. 22, 46–55.

Issa, R.I., 1986. Solution of implicitly discretized fluid flow equations by operator splitting. J. Comput. Phys. 62, 40–65.

Jalili, B., Jalili, P., 2023. Numerical analysis of airflow turbulence intensity effect on liquid jet trajectory and breakup in two-phase cross flow. Alex. Eng. J. 68, 577–585.

Jalili, B., Aghaee, N., Jalili, P., Ganji, D.D., 2022a. Novel usage of the curved rectangular fin on the heat transfer of a double-pipe heat exchanger with a nanofluid. Case Stud. Therm. Eng. 35, 102086.

Jalili, P., Kazerani, K., Jalili, B., Ganji, D.D., 2022b. Investigation of thermal analysis and pressure drop in non-continuous helical baffle with different helix angles and hybrid nano-particles. Case Stud. Therm. Eng. 36, 102209.

Ji, C., Liu, D., Waqas, H., Sun, S.L., Jalili, B., Abdelmohimen, M.A., 2024. Melting performance of Molten Salt with nanoparticles in a novel triple tube with leaf-shaped fins. Case Stud. Therm. Eng. 61, 105063.

Kwon, K., Kim, Y., Kwon, Y., Koseki, H., 2021. Study on accidental fire at a large-scale floating-roof gasoline storage tank. J. Loss Prev. Process. Ind. 73, 104613.

Li, J.C., Liu, M., Dang, S.W., Hu, L.C., Chen, G., Zhang, S.D., Xu, H., 2024. Numerical study on the influence of various design variables on the behavior characteristics of oil and gas in internal floating roof tanks. Energies 17, 4336.

Neyshabouri, H., Niasati, M., 2024. Analysis of the electromagnetic effects on the large floating roof oil tanks by nearby lightning strike based on TLM. J. Electrost. 129, 103927.

Oliveira, P.J., Issa, R.I., 2001. An improved PISO algorithm for the computation of buoyancy-driven flows. Numer. Heat Tran. B 40, 473–493.

Salehipour, D., Jalili, B., Jalili, P., 2024. Effect of humidification of combustion products in the boiler economizer with spiral geometry. Results Eng. 21, 101906.

Sun, W., Cheng, Q., Zheng, A., Gan, Y., Gao, W., Liu, Y., 2018. Heat flow coupling characteristics analysis and heating effect evaluation study of crude oil in the storage tank different structure coil heating processes. Int. J. Heat Mass Tran. 127, 89–101.

Sun, W., Liu, Y., Li, M., Cheng, Q., Zhao, L., 2023. Study on heat flow transfer characteristics and main influencing factors of waxy crude oil tank during storage heating process under dynamic thermal conditions. Energy (Calg.) 269, 127001.

Sun, S.L., Liu, D., Wang, Y.Z., Kim, H.B., Hassan, M., Hong, H.J., 2023a. Heat transfer performance prediction of Taylor–Couette flow with longitudinal slits using artificial neural networks. Appl. Therm. Eng. 221, 119792.

Sun, S.L., Liu, D., Wang, Y.Z., Qi, Y.L., Kim, H.B., 2023b. Convective heat transfer and entropy generation evaluation in the Taylor–Couette flow under the magnetic field. Int. J. Mech. Sci. 252, 108373.

Teng, Y.L., Li, R., Huang, J.,X., Jian, P., He, J., 2021. Influence of pier form on impact effect of debris flow slurry. Highw 66, 109–115.

Wang, F., 2004. Computational Fluid Dynamics Analysis, first ed. Qinghua University, Beijing.

Wang, M., Yu, B., Zhang, X., Yu, G., Li, J., 2018. Experimental and numerical study on the heat transfer characteristics of waxy crude oil in a 100000 m^3 double-roof floating roof oil tank. Appl. Therm. Eng. 136, 335–348.

Wang, M., Zhang, X., Shao, Q., Li, J., Yu, B., 2019. Temperature drop and gelatinization characteristics of waxy crude oil in 1000m^3 single and double-roof floating roofoil tanks during storage. Int. J. Heat Mass Tran. 136, 457–469.

Yang, H., Ren, B., Huang, Y., Zhang, Z., Hu, W., Liu, M., Hao, Z., 2024. Volatile organic compounds (VOCs) emissions from internal floating-roof tank in oil depots in Beijing: Influencing factors and emission reduction strategies analysis. Sci. Total Environ. 916, 170222.

Zhang, G., Huang, F., Huang, W., Zhu, Z., Fang, J., Ji, H., Sun, X., 2020. Analysis of influence of floating-deck height on oil-vapor migration and emission of internal floating-roof tank based on numerical simulation and wind-tunnel experiment. Processes 8, 1026.

Zhao, F., 2020. Analysis of damage causes and preventive measures for floating plate of internal floating roof storage tank. Chem. Manage. 3, 142–143.

Zhao, J., Wei, L., Dong, H., Liu, F., 2016. Research on heat transfer characteristic for hot oil spraying heating process in crude oil tank. Case Stud. Therm. Eng. 7, 109–119.

Zhao, J., Dong, H., Lei, Q., Guo, J., Wei, L., 2017. Research on heat transfer characteristic of waxy crude oil during the gelatinization process in the floating roof tank. Int. J. Therm. Sci. 115, 139–159.

Zhao, J., Liu, J., Dong, H., Zhao, W., Wei, L., 2020. Numerical investigation on the flow and heat transfer characteristics of waxy crude oil during the tubular heating. Int. J. Heat Mass Tran. 161, 120239.

Zhao, J., Li, M., Liu, S., Dong, H., 2024. Heat transfer characteristics of oil receiving and delivering process in crude oil storage tanks. Case Stud. Therm. Eng. 61, 104994.

Zhou, Q.Y., Li, B., Lu, Y., Chen, J., Shu, C.M., Bi, M.S., 2023. Dynamic risk analysis of oil depot storage tank failure using a fuzzy Bayesian network model. Process Saf. Environ. Prot. 173, 800–811.